High Winds Generated by Bow Echoes. Part II: The Relationship between the Mesovortices and Damaging Straight-Line Winds

ROGER M. WAKIMOTO

National Center for Atmospheric Research, Boulder, Colorado

HANNE V. MURPHEY

Department of Atmospheric Sciences, University of California, Los Angeles, Los Angeles, California

CHRISTOPHER A. DAVIS

National Center for Atmospheric Research, Boulder, Colorado

NOLAN T. ATKINS

Department of Meteorology, Lyndon State College, Lyndonville, Vermont

(Manuscript received 1 July 2005, in final form 10 January 2006)

ABSTRACT

Airborne radar analysis of a mesovortex that developed near the apex of a bow echo is presented. The mesovortex was shown to play a critical role in determining the location of intense "straight-line" wind damage at the surface. The perturbation pressure gradient force (in natural coordinates) along the parcel path accelerated the horizontal winds; however, intense mesovortices modified the low-level outflow and largely determined the locations where the strongest winds occurred. Regions of maximum winds are accounted for as a superposition of the vortex and the flow in which it is embedded. The strongest winds occur on the side of the vortex where translation and rotation effects are in the same direction. This model explains the observed tongue of high wind speeds that were confined to the periphery of the mesovortex. The origin of the mesovortex is also examined. Similarities and differences of this bow echo event with recent modeling studies are presented.

1. Introduction

The life cycle of the bow echo and its relationship with straight-line wind damage and tornadoes was first proposed nearly three decades ago (Fujita 1978). Subsequent investigations have revealed that this echo type is one of the more common modes of convective organization associated with severe weather (e.g., Fujita and Wakimoto 1981; Johns and Hirt 1987; Przybylinski 1995; Weisman 2001). There have been a number of attempts to simulate the bow echo in order to understand how a quasi-linear convective system evolves into a bow shape (e.g., Weisman 1992, 1993; Weisman and Davis 1998; Weisman and Trapp 2003; Trapp and Weisman 2003). However, there has been no comprehensive observational study that has captured the life cycle of a bow echo during the time that severe outflow winds were being produced (e.g., Schmidt and Cotton 1989; Jorgensen and Smull 1993). Burgess and Smull (1990), Przybylinski (1995), and Atkins et al. (2004, 2005), among others, have examined severe bow echoes using single-Doppler radar data. Atkins et al. (2005) combined a detailed damage survey with single-Doppler velocity data of a bow echo in order to document the relationship between tornadoes and straight-line wind damage. Fujita (1981) has presented the only known multi-Doppler wind syntheses of a bow echo while it was producing damaging winds at the surface. Unfortunately, his study was only for one analysis time and was confined to a single height.

Corresponding author address: Roger M. Wakimoto, NCAR/EOL, P.O. Box 3000, Boulder CO 80307.
E-mail: wakimoto@ucar.edu

A key question in past studies was documenting the mechanism(s) that produce intense outflow at the surface. The prevailing hypothesis was that an intense, descending rear-inflow jet [a characteristic feature that develops in the stratiform region of mesoscale convective systems (MCSs), e.g., see Smull and House (1987)] was responsible for the damaging winds. Detailed aerial and ground surveys, however, have revealed swaths of damage that appear to be too small to be attributed to a descending rear inflow (Fujita 1978, 1981; Fujita and Wakimoto 1981; Forbes and Wakimoto 1983; Funk et al. 1999). Fujita (1978), Burgess and Smull (1990), and Wakimoto (2001) have suggested that these smaller swaths of damage might be associated with downdrafts produced by individual thunderstorms within the convective line (i.e., microbursts).

In contrast, a novel hypothesis has been recently advanced by Weisman and Trapp (2003) and Trapp and Weisman (2003) based on numerical simulations of bow echoes. They suggest that the damaging winds at the surface were caused by strong mesovortices developing at the leading edge of the outflow boundary. The existence of these mesovortices is not surprising because it is well known that bow echoes can spawn tornadoes (e.g., Fujita 1978; Forbes and Wakimoto 1983; Wakimoto 1983; Atkins et al. 2004; Trapp et al. 2005). Trapp and Weisman (2003) propose that the mesovortices create mesolows via the fluid shear terms in the diagnostic perturbation pressure equation. The strong winds were, subsequently, driven by the horizontal pressure gradients created by these mesolows. To date, no detailed observational study has been undertaken that could confirm or refute this hypothesis.

A squall line developed over eastern Nebraska in the evening of 5 July 2003 during the Bow Echo and Mesoscale Convective Vortex (MCV) Experiment (BAMEX; Davis et al. 2004). An airborne Doppler radar was deployed on the convective system and was able to capture the transition of a quasi-linear convective system into a bow echo while it was producing straight-line wind damage rated greater than F1 in intensity (Fujita 1981) near Omaha, Nebraska. Wakimoto et al. (2006, hereafter Part I) documented the overall evolution of the 5 July storm, hereafter, referred to as the Omaha bow echo. The kinematic structure of the bow echo was superimposed on a detailed damage survey to relate the Doppler wind syntheses with intense winds at the surface. Several maxima of positive vertical vorticity along the gust front, suggesting the presence of mesovortices, were resolved in the dual-Doppler wind syntheses. These vorticity maxima appear to be closely associated with the strongest wind damage.

This paper reexamines the Doppler wind syntheses at much higher resolution than was presented in Part I. The objective is to relate the structure of mesovortices to the damaging winds produced by a bow echo. Accordingly, analyses over a smaller region (21 km $\times$ 21 km) were created in order to describe the kinematic structure near the apex of the bow echo. In particular, the life cycle of an intense mesovortex that developed at this location is shown. Section 2 briefly describes the airborne Doppler radar platform used in this study. A close examination of the evolution of an intense mesovortex and its relationship to damaging winds at the surface is presented in section 3. Section 4 examines the possible forcing mechanism of the strong winds, and section 5 describes the origin of mesovortices developing along the leading edge of the outflow boundaries. A summary and discussion is presented in section 6.

2. ELDORA

The primary data source for this study was data collected by an airborne Doppler radar called the Electra Doppler radar (ELDORA). The platform is maintained and operated by the National Center for Atmospheric Research (NCAR) and is mounted within the tail section of a Naval Research Laboratory (NRL) P-3. Further discussion of the radar parameters, scanning technique, and flight tracks is presented in Part I of this manuscript. The synthesis of the Doppler velocities into a three-dimensional wind field presented in this paper is discussed in the appendix. The radar data were interpolated onto a finer grid because the segment of the convective line under investigation was confined to a smaller region than was shown in Part I.

3. The evolution of the mesovortex near the apex and its relationship to surface damage

Part I of this study presented analyses that examined a substantial portion ($\sim$90 km) of a quasi-linear convective system. While this domain is appropriate to document the overall storm structure, the details of the relationship between the mesovortices and surface damage could not be ascertained. Accordingly, this section presents analyses over a smaller region indicated by the small black boxes that were drawn on Figs. 10, 12, 14, and 15 in Part I in order to describe the kinematic structure near the apex of the bow echo.

a. 0510:01–0522:20 UTC

The first pass near the MCS was executed between 0510–0522 UTC. As discussed in Part I, the storm was

entering the western section of Omaha and the storm outflow resulted in sporadic damage rated <F0 on the Fujita scale (Fujita 1981). The intense convection was quasi linear at this time because the system had not yet entered the "bowing" stage. The region depicted in Fig. 1a shows a segment of the line where the bow apex will form in subsequent analyses.

The gust front is shown by the line of convergence (indicated by the red arrows) evident in the ground-relative wind field and the single-Doppler velocity plot at 300 m above ground level (AGL; hereafter, all heights are AGL). The position of the gust front can also be identified in the radar reflectivity plot as a thin line of radar reflectivity (Wilson and Schreiber 1986). There were updrafts along the gust front with peak values exceeding 12 m s^{-1}. The gust front was also distorted into an S-shaped pattern (note the region characterized by 0 m s^{-1} in single-Doppler velocity). This type of distortion of a frontal boundary is frequently associated with a mesocirculation or mesovortex. Indeed, a maximum in cyclonic vorticity $>12 \times 10^{-3}$ s^{-1} (indicated by the "X") is positioned near the center of the S pattern. A smaller vorticity maximum is located ~5 km to the north along the gust front.

The red dots labeled on the single-Doppler velocity image denote two extensions of strong velocities toward the radar (indicated by the areas colored light blue). The proximity of these high-velocity pockets to the mesovortices along the gust front suggests that there may be a relationship between strong winds and vorticity centers as suggested by Trapp and Weisman (2003). The isotachs of horizontal velocity (shown by the white lines) in Fig. 1a reveal that the strongest winds within the cold pool are >40 m s^{-1} and located ~12 km to the west of the frontal boundary. The dashed red line denotes the position of the damage/no-damage boundary (refer to Figs. 5 and 10 in Part I). Accordingly, most of the region encompassed by the box shown in the Fig. 1a was devoid of surface damage.

A west–east vertical cross section through the center of the developing mesovortex is presented in Fig. 2a. The strongest vertical vorticity is near the surface and centered at the thin line. The circulation tilts westward with increasing height but only extends a few kilometers above the surface. These characteristics are consistent with the numerical results presented by Weisman and Trapp (2003).

b. 0524:20–0536:21 UTC

The MCS was in the early stages of forming a bow-shaped echo during the subsequent analysis time (Fig. 1b). Damage at the surface was occurring over an extensive region and was rated between F0 and F1. The mesovortex was located to the north of the apex of the bow and had strengthened at this time ($>18 \times 10^{-3}$ s^{-1}). A closed circulation is apparent in the storm-relative wind field and a rotational couplet in the single-Doppler plot is collocated with the mesovortex (the couplet was also evident in the radar analysis presented in Part I). The isotachs and single-Doppler velocities illustrate that the gradient of velocity on the cold-air side of the outflow boundary was increasing to the south of the mesovortex. Another well-defined mesovortex is located ~12 km to the northeast of the primary circulation.

The updrafts along the gust front had intensified but were segmented in Fig. 1b. Comparison with the vertical vorticity plot reveals that the mesovortices are positioned in the weak updraft regions. The relationship between vertical velocity and vorticity along an outflow boundary has been documented by Mueller and Carbone (1987). Intense rotation produces low pressure owing to the fluid shear terms in the perturbation pressure equation (Klemp and Rotunno 1983). A downward-directed pressure gradient force develops if the rotation is strongest at the surface. As a result, the updrafts will be suppressed or a downdraft may develop in these regions. These findings were also shown by Weisman and Trapp (2003) and Trapp and Weisman (2003).

Another feature that is apparent in the vertical vorticity analysis is the tendency to form a vortex couplet at the leading edge of the outflow. Indeed, both cyclonic vortices are accompanied by a weaker region of anticyclonic vorticity ($<-6 \times 10^{-3}$ s^{-1}) located a few kilometers to the north. While the cyclonic vortices are positioned along the gust front, the anticyclonic vortices are displaced to the west, within the cold air. It should be noted that a vortex couplet associated with the main mesovortex was also apparent in Fig. 1a.

A major change in the kinematic structure of the mesovortex is evident in the west–east vertical cross section shown in Fig. 2b. Recall, that the quasi-linear convective system was beginning to "bow out" at this stage. The bulging and acceleration of the echoes was in response to an intensifying and descending rear-inflow jet. The mesovortex is embedded within an updraft and now appears to extend to 7–8 km. The circulation has also intensified via vortex stretching with the peak values $>20 \times 10^{-3}$ s^{-1} at 3 km. The intense outflow at low levels is evident by the pronounced tilt in the mesovortex with height.

c. 0538:00–0548:26 UTC

Strong outflow winds were creating damage at the surface rated >F1 during the third pass of ELDORA by the storm (Fig. 1c). The radar reflectivity data pre-

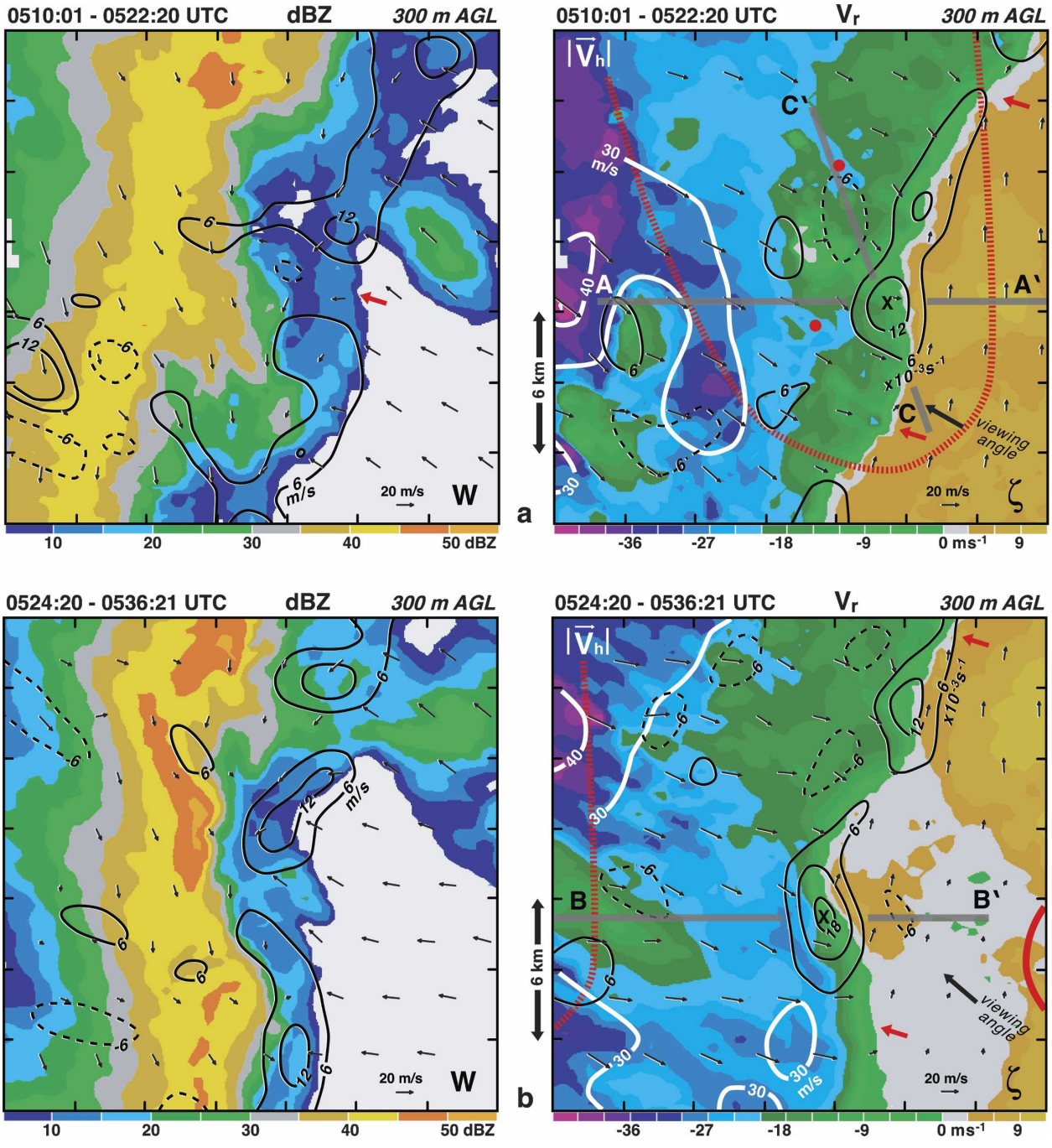

FIG. 1. Dual-Doppler wind syntheses at (a) 0510:01–0522:20, (b) 0524:20–0536:21, (c) 0538:00–0548:26, and 0549:56–0602:23 UTC at 300 m AGL. Storm-relative winds, and vertical velocities are superimposed onto radar reflectivity. Ground-relative winds, vertical vorticity, and isotachs of horizontal velocity are superimposed onto single-Doppler velocities. Perturbation pressure is superimposed onto the radar reflectivity in (c). The red dots on the single-Doppler velocity plot in (a) denote the locations of two regions of high wind speed. The red arrow on the radar reflectivity plot in (a) indicates the position of thin line. The red arrows on the single-Doppler velocity plot in (a) and (b) denote the location of a convergence line at the leading edge of the outflow. East–west gray lines in (a) and (b) indicate the position of the vertical cross sections shown in Fig. 2. Approximate north–south gray line in (a) indicates the position of a vertical cross section shown in Fig. 7. The gray line in (c) represents the trajectory of a parcel that is associated with the strongest winds at 300 m AGL and within the area rated Fl in damage intensity. The parcel times are listed along the path. The dotted line in (c) and (d) represents the flight track of the NRL P-3. Surface wind report from Harlan, Iowa (HNR) is shown on the single-Doppler velocity plot in (d). The damage at the surface is based on the damage survey and is shown by the dashed red (damage/no-damage boundary), solid red (F0 contour), and magenta (F1 contour) lines plotted on the single-Doppler velocities. The location of the syntheses is shown in Figs. 10, 12, 14, and 15 in Part I.

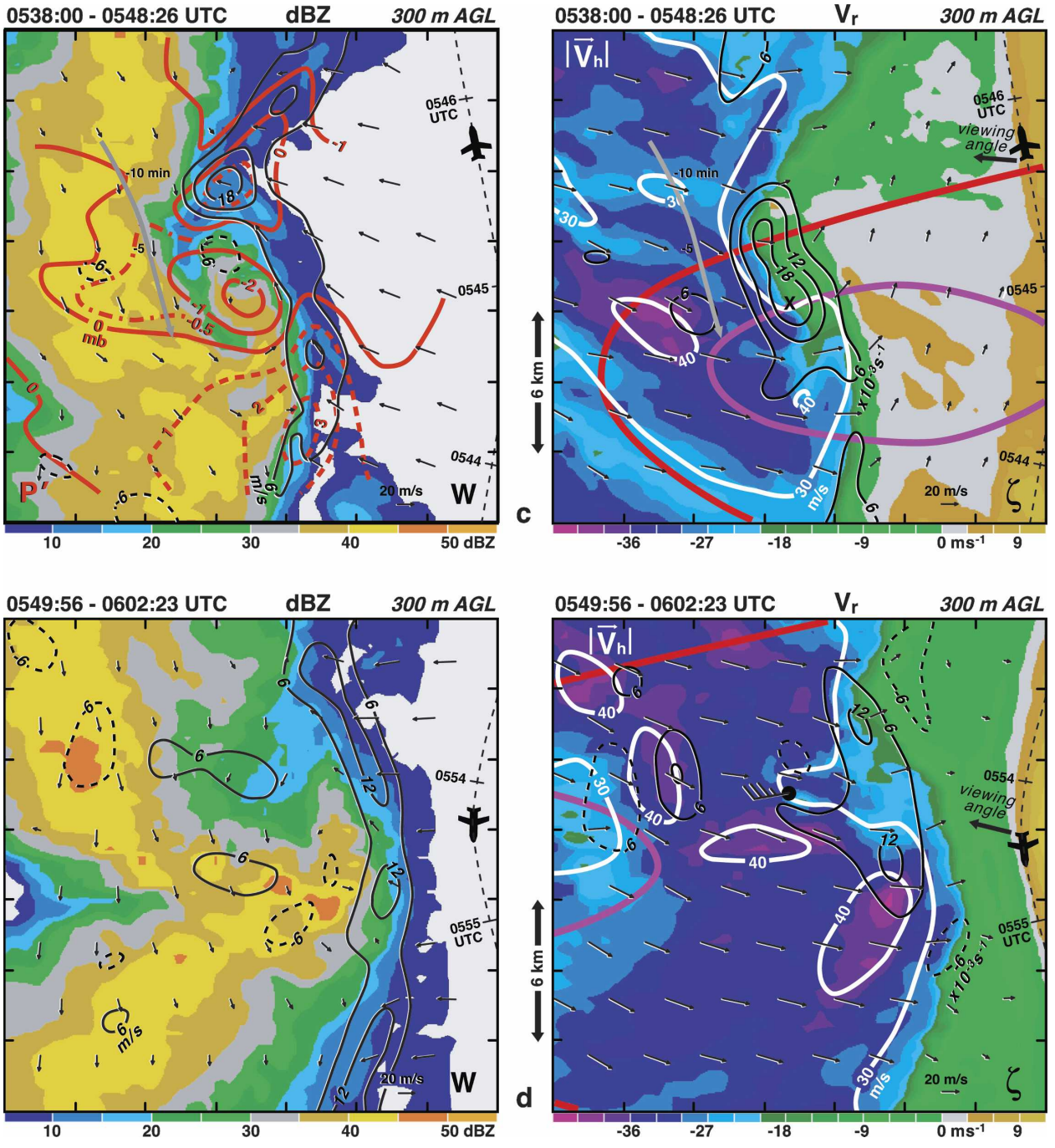

FIG. 1. (*Continued*)

sented at a coarser resolution in Part I suggested a hook-like feature formed at the bow apex. This is confirmed with the higher-resolution analysis presented in Fig. 1c. A well-defined hook echo with a diameter of ~9 km is apparent in the figure. The mesovortex has entered its most intense phase and a pronounced circulation can be identified in the storm-relative wind field. The mesovortex is not centered within the F1 contour but is displaced to the north. The 30 m s^{-1} isotach outlines a pronounced tongue of high wind speeds that is wrapping around the western and southern periphery of the mesovortex in Fig. 1c. Peak wind speeds >40 m s^{-1} are now close to the leading edge of the outflow and within the F1 isopleth. The westerly ground-

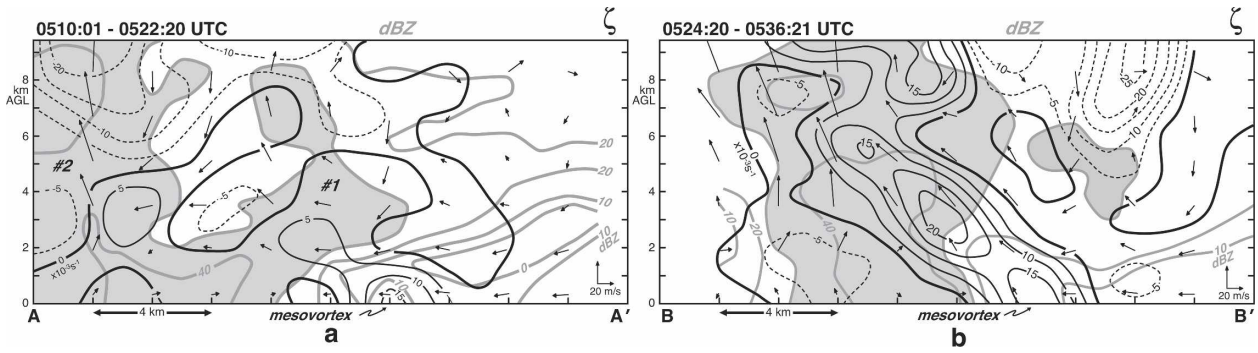

FIG. 2. West–east vertical cross sections through the mesovortex at (a) 0510:01–0522:20 and (b) 0524:20–0536:21 UTC. Gray lines are radar reflectivity with values greater than 30 dB*Z* shaded gray. Black and dashed lines are positive and negative vertical vorticity values, respectively. The storm-relative winds in the plane of the cross section are plotted. The location of the cross sections is shown in Figs. 1a and 1b.

relative flow in the area of most intense damage is consistent with the vectors plotted in Fig. 5b in Part I. Atkins et al. (2005) has presented single-Doppler velocity data that suggest that there is a displacement between the mesovortex and the region where the strongest damage occurs (see their Fig. 8).

d. 0549:56–0602:23 UTC

A spearhead echo (Fujita and Byers 1977; Fujita 1985) formed at the apex of the bow echo during the fourth analysis time as shown in Fig. 1d. The single-Doppler velocities and wind syntheses shown in the figure suggest that the low-level flow was strongest at this time. However, the aerial and ground survey superimposed onto the analyses illustrates that the most intense winds had weakened. The damage intensity was rated between F0 and F1. These results provide further evidence concerning the tenuous relationship between the strongest single-Doppler velocities at low levels and surface damage. Accordingly, it can be challenging to pinpoint the exact areas that are susceptible to damaging winds using an operational Doppler radar.

4. The origin of the strong surface winds

Trapp and Weisman (2003) hypothesize that the horizontal pressure gradients produced by the mesovortices in their simulations are important in creating regions of high speeds that could produce damage. To test this hypothesis, the perturbation pressure field was retrieved from the Doppler wind syntheses using a technique first proposed by Gal-Chen (1978). An explanation of the retrieval technique is described in the appendix.

The retrieval for the 0538–0548 UTC wind field at 300 m is shown in Fig. 1c. The gust front, except at the location of the mesovortex, is characterized by a ridge of high perturbation pressure owing to the fluid extension terms in the diagnostic pressure equation (i.e., strong horizontal convergence at the frontal boundary). The mesovortex was accompanied by a mesolow with a minimum perturbation pressure <-2 mb that was centered at the tip of the hook echo. A retrieval of the cyclostrophic component of the perturbation pressure in the storm-relative field (not shown) reproduces the mesolow pattern shown in Fig. 1c. Accordingly, the mesovortex was primarily in cyclostrophic balance.

Backward trajectories that terminated near the tip of the tongue of high wind speeds (outlined by the 30 m s^{-1} isopleth in Fig. 1c) were calculated in order to isolate the possible forcing mechanism. The 0510–0522, 0524–0536, and 0538–0548 UTC Doppler wind syntheses were used in the trajectory analysis. The dual-Doppler velocities were linearly interpolated between time steps (10 s) and a fourth-order Runge–Kutta method was used to determine the grid points for each step of the path. Air parcels at the lowest grid level were released every 10° in a circle whose radius was varied between 1 and 2 km. All parcels essentially followed parallel paths. Accordingly, the track shown in Fig. 1c was selected as the one that best represented the mean path of the tracks. Selecting another parcel path, however, would not have altered the conclusions presented in this section.

The height of the parcel for the preceding 13 min was <500 m (Fig. 3a), suggesting that the strong winds did not originate from higher levels and descend within a thunderstorm downdraft. This would discount outflow from a microburst as a causal mechanism for the damaging surface winds. The observed values of horizontal wind speed show a continual increase in the speed during the last ~5 min along the parcel path (Fig. 3b). Also shown at the top of Fig. 3b is the component of the

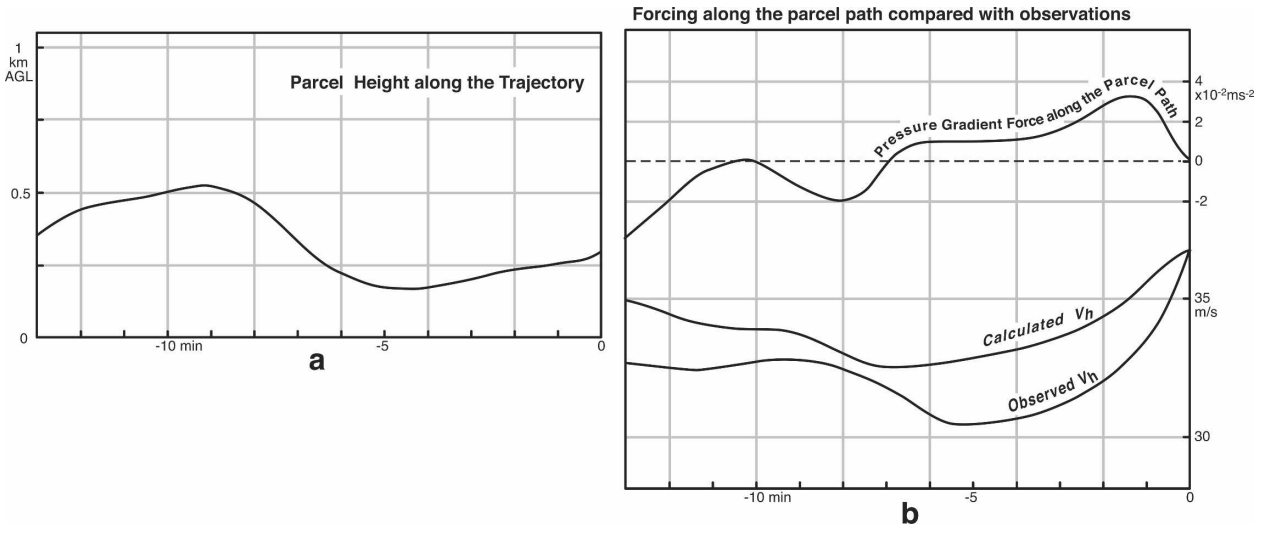

FIG. 3. Backward trajectory for a representative parcel that lies within the peak outflow winds at low levels. (a) Observed parcel height along the trajectory. (b) Observed and calculated horizontal wind speed along the trajectory and the pressure gradient force along the trajectory. Parcel path is shown in Fig. 1c.

perturbation pressure gradient force in natural coordinates (hereafter; referred to as pressure gradient force) along the parcel path. Using the observed horizontal wind speed at the end of the parcel trajectory, a backward Lagrangian calculation of the wind speed based solely on the contribution of the pressure gradient force was determined. The result is labeled as the "calculated horizontal wind speed" in the figure. Although the two plots are not identical, the similar shapes of the observed and calculated curves suggest that the pressure gradient force is important in generating high wind speeds in bow echoes. This appears to substantiate the hypothesis advanced by Trapp and Weisman (2003). The most likely reason that the pressure gradient force overestimates the actual acceleration is owing to the neglect of turbulent mixing, which will systematically reduce the magnitude of localized jets. It is also possible, however, that the overestimation is a result of the budget imbalance associated with the coarse time resolution between the wind syntheses.

A closer examination of the wind field in Fig. 1c, however, suggests that the pressure forces alone do not fully explain the observed pattern of high winds near the surface. The parcel trajectory would be expected to terminate closer to the center of the mesolow if the pressure gradients created by the mesolow dominated. Instead, the parcel skirts around the periphery of the mesolow (this path is largely a consequence of the cyclostrophically balanced flow within the mesovortex mentioned earlier). Further evidence is the tongue-shaped structure of the 30 m s^{-1} isotach in Fig. 1c, which wraps around the mesovortex and mesolow. Parcels that terminated near the center of the mesolow were examined in order to assess their origin. The vertical pressure gradient force (downward pointing) dominated in this region because the minimum perturbation pressure within the mesolow was located near the surface. As a result, the parcels descended from aloft in a spiral manner. These air parcels were not responsible for generating the strongest damaging winds shown in Fig. 1c even though they were located near the region of strong *horizontal* pressure gradients.

The displacement of the high wind speeds (and damage) to the southern flank of the mesovortex is consistent with the superposition of a vortex and the flow in which it is embedded. This type of asymmetry is commonly observed during poststorm surveys of tornado and hurricane damage. The strongest winds typically occur on the side of the vortex where translational and rotational effects are in the same direction (e.g., Shea and Gray 1973; Fujita 1981; Holland 1987; Wakimoto and Black 1994).

An attempt was made to determine whether a vortex superposition onto the flow could account for the wind field shown in Fig. 1c. The Poisson equation for the perturbation streamfunction ($\nabla^2\psi' = \zeta$) was solved assuming that the vertical vorticity was zero everywhere outside of the mesovortex and that the perturbation streamfunction was equal to zero on the lateral boundaries. This boundary condition required the use of the Doppler wind syntheses over the large domain described in Part I. The retrieved streamfunction was used to compute the nondivergent component of the wind field. These winds were subsequently subtracted

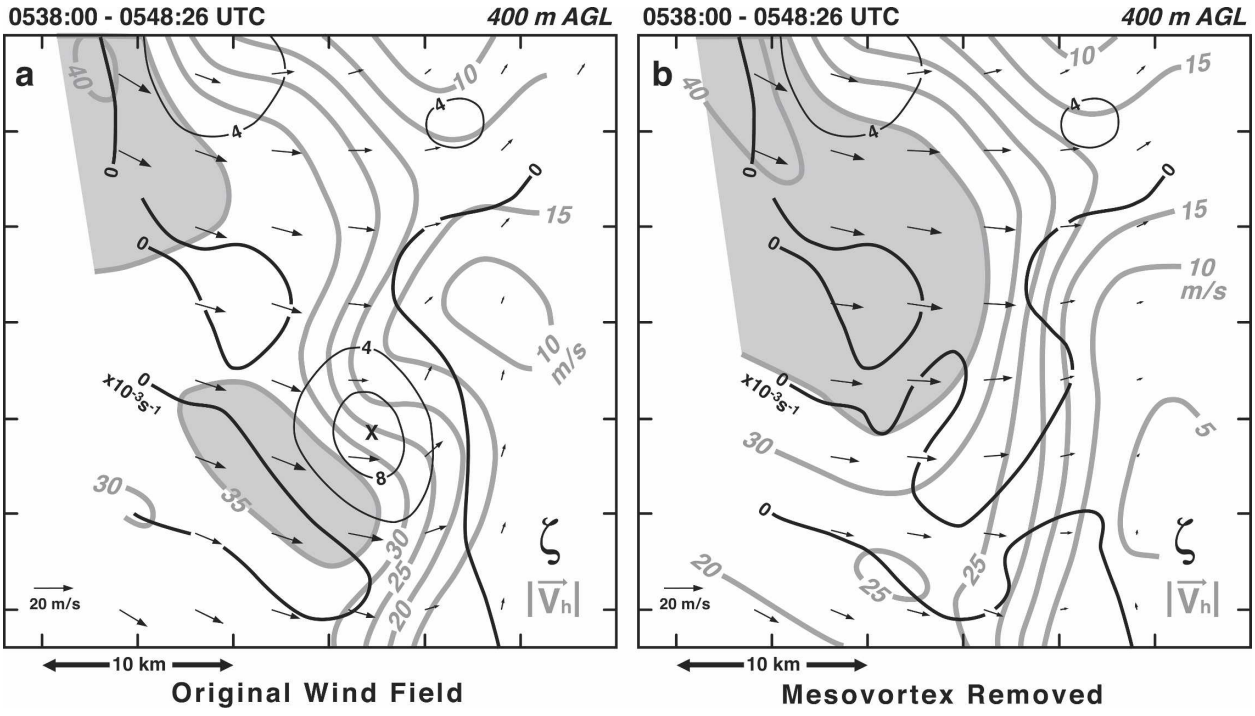

FIG. 4. Doppler wind syntheses at 0538:00–0548:26 UTC at 400 m AGL superimposed onto vertical vorticity, isotachs, and the ground-relative Doppler wind synthesis (a) for the original analysis and (b) with the circulation associated with the mesovortex removed. Black and gray lines are vertical vorticity and isotachs, respectively. Areas shaded gray are >35 m s^{-1}.

from the Doppler wind syntheses to create a modified wind field without the effect of the mesovortex. The result of these calculations is presented in Fig. 4. The impact of the mesovortex is illustrated by comparing the two plots shown in the figure. The pocket of high winds (>35 m s^{-1}) responsible for the F1 damage on the southern periphery of the mesovortex has been removed in Fig. 4b. The strongest postfrontal winds are now displaced much farther to the north and appear to be a result of the descending rear-inflow jet, as would be expected. This analysis suggests that the high winds noted during this time were largely accounted for by the superposition of the mesovortex on the flow.

Another segment of the convective line was examined based on data collected during the 0549:56–0602:23 UTC analysis time (Fig. 5). A small bow-shaped echo developed at this location and was associated with microburst damage at the surface. The area affected by the microburst is highlighted by the circular F0 contour. Confirmation that this region was affected by damaging microburst winds is revealed by the pocket of strong, negative single-Doppler velocities (<-42 m s^{-1}) in Fig. 5 that are near the F0 contour (also shown by the 40 m s^{-1} isotach of ground-relative winds).

A region of cyclonic vertical vorticity is displaced to the northern part of the F0 contour and no closed circulation could be identified in the storm-relative wind field. In addition, the peak cyclonic vorticity values were weaker than those presented in Fig. 1c. Similar to the earlier discussions, a trajectory that best represents the mean path of all tracks through the region characterized by damage intensity >F0 is drawn on the figure. The parcel passes through a rear-inflow notch, that is, a notch that forms along the trailing edge of the convective line and usually indicates where the downburst/microburst winds are the strongest (Przybylinski 1995). A mesolow is apparent in the perturbation pressure field but it is not as distinct as the previous example (Fig. 5). The parcel trajectory skirts to the south of the minimum in perturbation pressure instead of through the center of the mesolow.

The results presented in this paper support the dominant role that mesovortices play in determining where the strongest wind damage associated with bow echoes is located. The pressure gradient force is nonnegligible because it is the only term in the momentum equation that can accelerate the wind. However, the analysis shown in Fig. 4 strongly suggest that the mesovortices produce preferred regions of damaging low-level winds that can best be described as a superposition of the circulation and the flow in which it is embedded. This

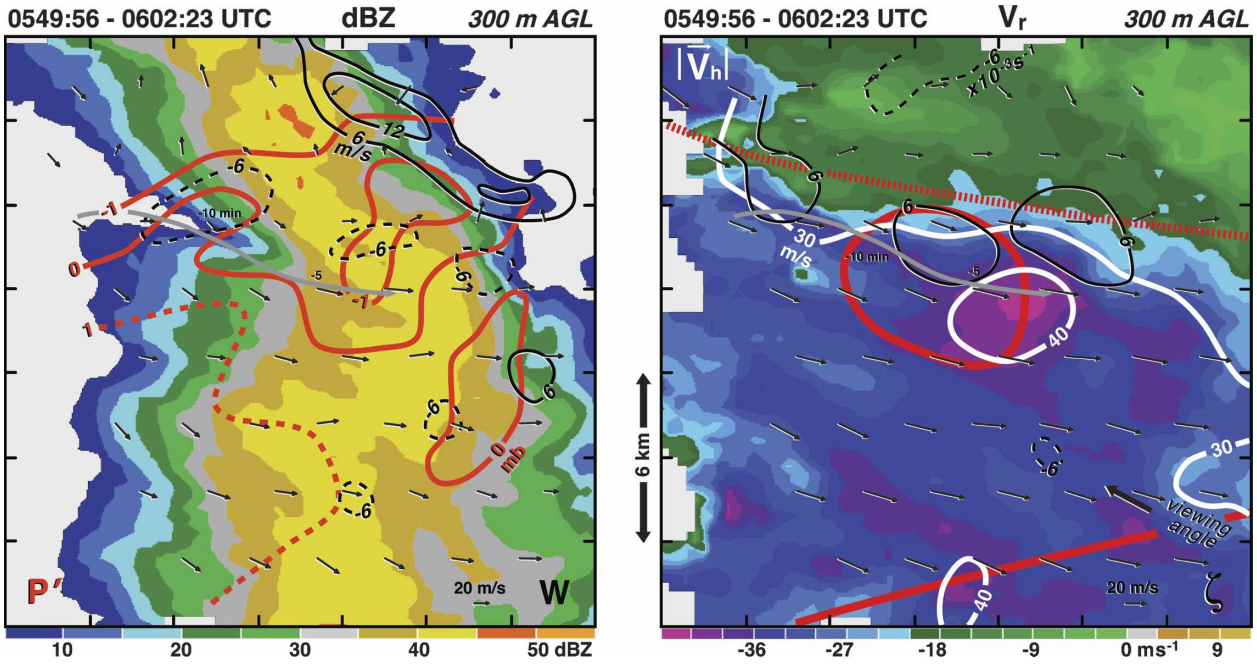

FIG. 5. Dual-Doppler wind syntheses at 0549:56–0602:23 UTC at 300 m AGL. Storm-relative winds, vertical velocities, and perturbation pressure are superimposed onto radar reflectivity. Ground-relative winds, vertical vorticity, isotachs of horizontal velocity are superimposed onto single-Doppler velocities. The damage at the surface is based on a survey and is shown by the dashed red (damage/no-damage boundary), and solid red (F0 contour) plotted on the single-Doppler velocities. The gray line represents the trajectory of a parcel that is associated with the strongest winds at 300 m AGL. The viewing angle of the Doppler radar is shown on the single-Doppler velocity plot. The location of the synthesis is shown in Fig. 15 in Part I.

model explains the tongue of high wind speeds that is confined to the periphery of the mesovortex (Fig. 1c). Removal of the mesovortex (as illustrated in Fig. 4) results in a displacement of the high winds to another location and over a larger region. Key signatures for forecasters to be aware of are "S shaped" patterns along the gust front in the single-Doppler velocity field, which frequently indicate developing mesovortices. In addition, small convex regions in the convective line may also form in response to a strong mesovortex. The area susceptible to damaging straight-line winds will be displaced from the center of the mesovortex in a region where the flow associated with the circulation is in the same direction as the movement of the convective line.

5. The origin of the vortex couplet

The origin of couplets of vorticity of the type documented in Figs. 1a and 1b is investigated in this section. Trapp and Weisman (2003) propose that the couplets are initiated at low levels by the tilting in precipitating downdrafts of crosswise horizontal baroclinic vorticity produced at the leading edge of the cold pool. The cyclonic vortex eventually dominates owing to the stretching of planetary vorticity.

The tilting and stretching of vertical vorticity were calculated in the present case in an attempt to understand the generating mechanism of the vortex couplet (Fig. 6). The first Doppler wind synthesis (0510–0522 UTC) was selected in order to examine the vortex genesis stage of the couplet discussed in section 3a. The analysis in Fig. 6a suggests that the anticyclonic and cyclonic vorticity centers are a result of downward tilting of horizontal vorticity. Stretching supports the continued strengthening of both circulations (Fig. 6b).

An approximate north–south cross section through the vortex couplet is presented in Fig. 7. A new cell that has initiated over the outflow boundary is dominated by updrafts as it continues to intensify (Fig. 7a). This cell is also apparent in the east–west cross section shown in Fig. 2a (labeled 1 on the radar reflectivity plot). Another updraft is located to the south of the cell (i.e., on the left-hand side of Fig. 7a) and is a component of the forced uplift at the leading edge of the outflow boundary.

A pronounced downdraft is positioned between the two updrafts and the anticyclonic and cyclonic vorticity features located near the surface. The location of the downdraft suggests that the tilting of horizontal vorticity is important in initiating mesovortices as suggested

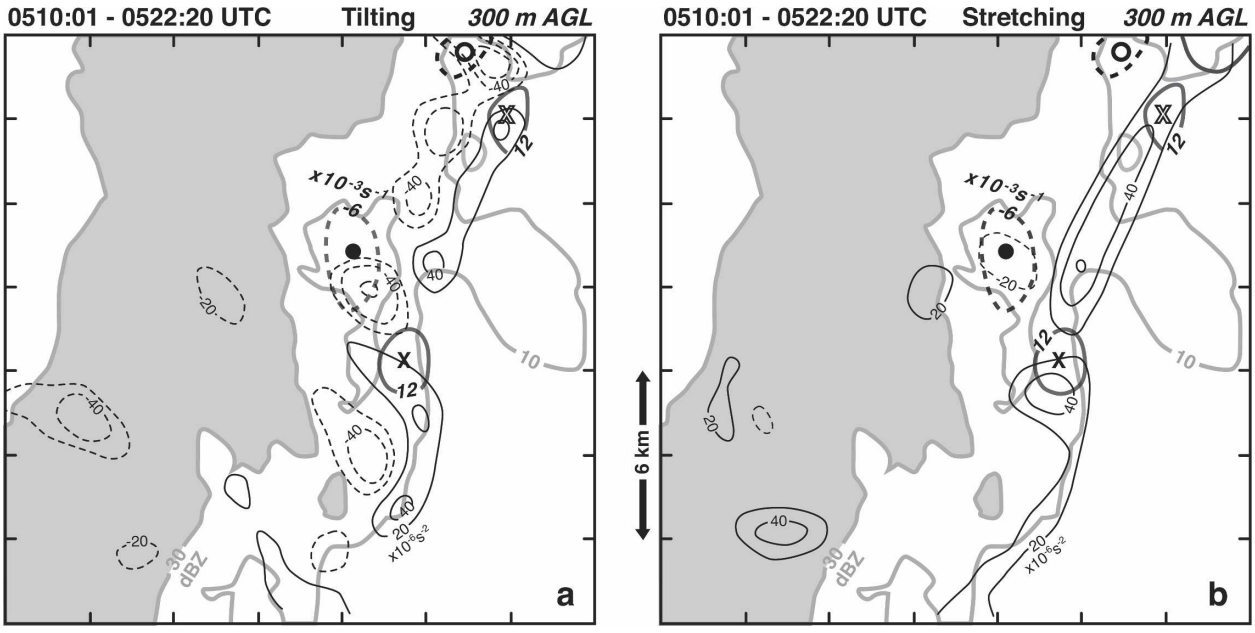

FIG. 6. (a) Tilting and (b) stretching terms of vertical vorticity for 0510:01–0522:20 UTC. Thin black and dashed lines in (a) and (b) represent positive and negative values of tilting and stretching, respectively. Light gray lines are radar reflectivity with values greater than 30 dBZ shaded gray. The black dot and cross represent the location of the anticyclonic and cyclonic vorticity centers that were shown in Fig. 1c. The 12 and -6×10^{-3} s^{-1} isopleths of vertical vorticity are plotted on the figure to highlight the couplet location.

by Trapp and Weisman (2003). Indeed, the relationship between the downdraft (Fig. 7a) and the orientation of the vorticity vectors at the lowest level in the cross section (Fig. 7b) point to vortex tilting in the generation of the couplet. Low-level plots of horizontal vorticity (not shown) reveal that the component of vorticity that is being tilted in Fig. 7b is the baroclinically produced circulation at the leading edge of the cold pool. Tilting by a downdraft of this latter horizontal vorticity would produce anticyclonic vertical vorticity to the north of the cyclonic vorticity as proposed by Trapp and Weisman (2003). Interpretation of the vorticity vectors above the lowest level in Fig. 7b is complicated by the existence of environmental horizontal vorticity above the cold pool and circulations produced by the convection. Environmental vorticity is created by the ambient wind shear and is represented by a vector that often points in the opposite direction of the horizontal vorticity generated within the cold pool (e.g., Rotunno et al. 1988; Weisman and Davis 1998).

Additional evidence that is consistent with this mechanism can be identified by comparing Figs. 1a, 1b, and 6. The northeast sector of Fig. 6a is dominated by two bands of positive and negative tilting. The bands are being produced by downdrafts (not shown) that are tilting the baroclinically produced horizontal vorticity vector. No vorticity couplet is apparent in this region at this time (Fig. 1a). However, a couplet does develop in this area by the next analysis time (northeast corner of Fig. 1b) with an orientation consistent with the tilting pattern (Fig. 6a). The location of this new vorticity couplet has been superimposed on the tilting and stretching pattern from the previous analysis to highlight this relationship (Fig. 6a, the open circle and cross). Moreover, the region where that cyclonic vortex will develop is embedded in a zone of positive stretching (Fig. 6b). Accordingly, an examination of the terms that predict the tendency of the vertical vorticity in the northeastern domain shown in Fig. 6 suggests that a vorticity couplet could develop in this region with the cyclonic member being more intense. This appears to be the case in Fig. 1b.

A difference in the schematic model of the initiation of the mesovortices shown by Trapp and Weisman (2003) is the origin of the downdraft. They propose that the downdraft is produced by precipitation. Analysis presented in Figs. 2a and 7a reveal that the cell forming above the outflow boundary is still growing and dominated by updrafts. The downdraft is clearly developing within weak radar reflectivities, an indication that the downdrafts were not forced by precipitation loading. Instead, these downdrafts are mechanically forced (e.g., Heymsfield and Schotz 1985; Raymond et al. 1991; Yuter and Houze 1995). This mechanism is a result of the pressure gradient forces required to maintain mass continuity in the presence of buoyant parcels (see

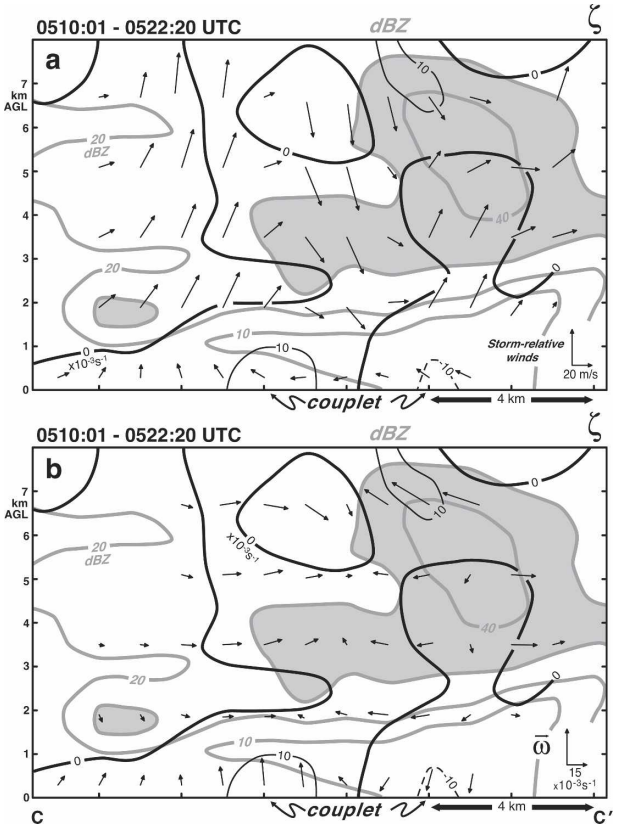

FIG. 7. Approximate north–south cross section through the vortex couplet at 0510:01–0522:20 UTC. (a) Radar reflectivity, storm-relative winds, and vertical vorticity, and (b) radar reflectivity, component of vorticity in the plane of the cross section (black arrows), and vertical vorticity. The location of the cross section is shown in Fig. 1a. Gray lines are radar reflectivity with values greater than 30 dB*Z* shaded gray. Thin black and dashed lines are positive and negative values of vertical vorticity, respectively.

Houze 1993). These downdrafts can be intense but often do not reach the surface (Knupp and Cotton 1985). Fortunately, the downdrafts only need to penetrate the top portion of outflow boundary in order to tilt the horizontal vorticity into the vertical, which appears to be the case in Fig. 7a.

Further evidence of the mechanically forced nature of the downdraft can be seen on either side of the echo labeled 1 in Fig. 2a. In retrospect, it is not surprising that these developing cells are unable to produce precipitating downdrafts near the gust front. The cells would be entering their mature stage well behind the leading edge of the cold pool (e.g., see the cell labeled 2 in Fig. 2a, which appears to be raining). It should be noted that this conclusion is based on a single case study and does not rule out other possible mechanisms that can produce vortex couplets.

Horizontal shear instability has frequently been cited as a causal factor in creating vorticity maxima along convergence boundaries (e.g., Carbone 1982; Mueller and Carbone 1987; Wakimoto and Wilson 1989; Lee and Wilhelmson 1997). Linear theory predicts that the fastest growing mode for this instability will be at a wavelength ~7.5 times the transition zone width (Miles and Howard 1964). The raw single-Doppler velocity data were examined in order to estimate the shear zone width across the gust front. The average width and standard deviation were 3.4 and 0.8 km, respectively. Accordingly, the most unstable wavelength would be between 19.5 and 31.5 km. The vertical vorticity analyses shown in Part I suggest that the major cyclonic maxima are approximately separated by these distances (see Figs. 10, 12, 14, and 15 therein). However, finer-resolution data presented in this paper reveal closer spacing as shown in Fig. 1b. In addition, the tendency for vortex couplets to develop along the gust front rather than circulations of the same sign would appear to rule out horizontal shearing instability as the initiation mechanism (also noted by Trapp and Weisman 2003).[1]

6. The Storm Lake bow echo

The results presented in section 4 suggest that mesovortices play an important role in the generation of high winds. The generality of the conclusions was examined by analyzing another bow echo event that occurred during BAMEX. The conditions that would support bow echoes existed over Nebraska and Iowa in the evening of 23 June 2003. Convection initiated over northeastern Nebraska at ~0030 UTC and organized into a quasi-linear convective system by 0300 UTC. The system evolved into a bow echo in northwestern Iowa during the time that numerous reports of fallen trees and roof damage were received by the National Weather Service.

Aerial and ground surveys were undertaken to determine the extent of the damage caused by the storm, which is referred to as the Storm Lake bow echo. A map based on the survey is presented in Fig. 8. The flow arrows reveal that the strongest winds were generally

[1] It should be noted, however, that numerical simulations by Lee and Wilhelmson (1997) reveal horizontal shear instability occurring at roughly half the theoretical prediction of Miles and Howard (1964). They state that the size and amplitude of the initial triggering instabilities play a major role in determining the separation of the initial mesocirculations along the shear zone. Accordingly, reducing the theoretical wavelength by half (i.e., 8.75–15.75 km) results in closer agreement with the observed mesovortices noted in the present study.

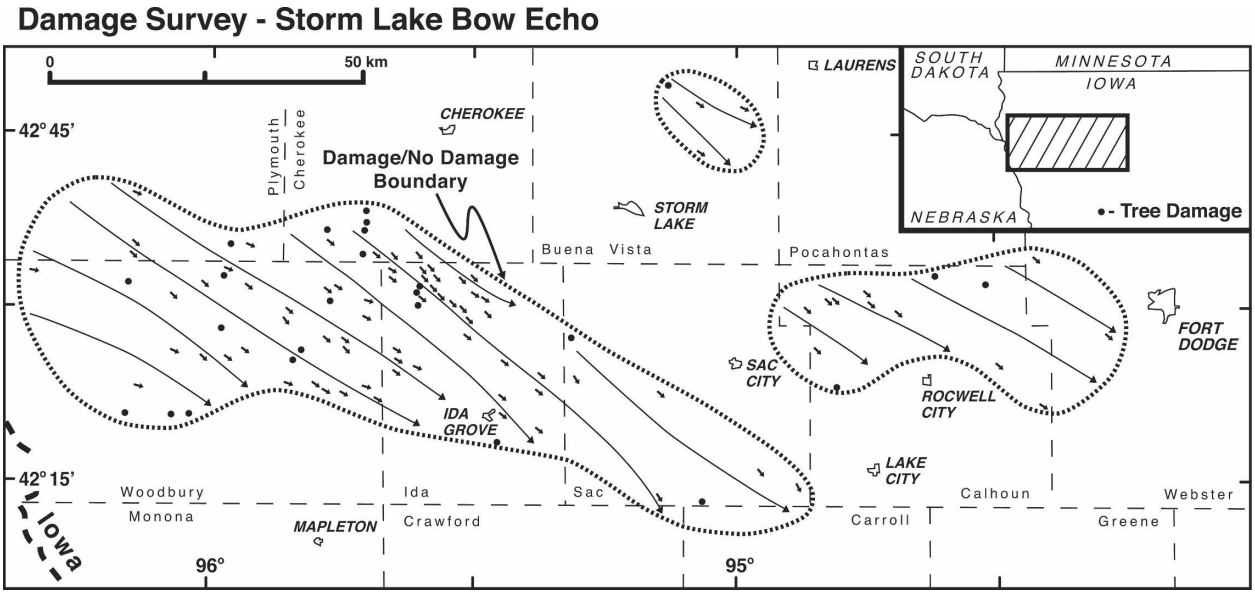

FIG. 8. Map of the surface damage produced by the Storm Lake bow echo. The map was compiled based on aerial and ground surveys throughout the region. The location of the map is shown by hatched box in the inset shown at the top right of the figure. The flow lines represent the direction of fallen trees or structural damage (black arrows represent the individual vectors of damage to trees or structure). The black dots represent damage to trees but no direction could be determined. The extent of the confirmed damage is indicated by the dashed line.

from a northwesterly direction. The surface damage was not as severe when compared to the survey in the aftermath of the Omaha bow echo shown in Part I. Indeed, no region was rated F0 or greater in intensity. The damage covered a wide region ~50 km wide and 150 km long; however, it was not a continuous swath of damage. Three separate regions of damage were identified during the survey with the largest area located southwest of Storm Lake.

The radar reflectivity data from the Des Moines, Iowa (DMX), Weather Surveillance Radar-1988 Doppler (WSR-88D) at 0622 and 0637 UTC are shown in Fig. 9. A gust front is apparent as a thin line of radar reflectivity. Also plotted are the surface weather data and the damage/no-damage boundary based on the results presented in Fig. 8. There is substantial cooling and an approximate 180° shift in wind direction from southeasterly to northwesterly after the passage of the outflow boundary at each surface station.

The track of the NRL P-3 is drawn in Fig. 9 and represents 2 of 15 flight legs past the storm. An inspection of the damage contours superimposed onto the radar reflectivity plot reveals that the production of strong surface winds was nearly over at this time. However, the data collected during this period were of primary interest because a well-defined mesovortex was identified along the outflow boundary.

The evolution of the mesovortex was captured in three consecutive wind syntheses using data collected with ELDORA. The Doppler radar methodology is the same as the one used to analyze the Omaha bow echo. The synthesis from 0628 to 0642 UTC was selected because it represents the time when the mesovortex attained its peak intensity (Fig. 10). A segment of the convective line has assumed a bow-like structure and a rear-inflow notch has formed behind the apex (Fig. 10a). The bow structure and a large pocket of strong, negative Doppler velocities associated with the descending rear-inflow jet are centered within the damage contour. The red arrow in Fig. 10b denotes the position of a cusp in the single-Doppler velocities, indicating the presence of circulation.

An enlargement of the wind synthesis in the region of the cusp feature is presented in Fig. 11. The updrafts are segmented along the gust front, similar to results shown in Fig. 1. A mesovortex near the cusp can be identified in the storm-relative wind field and the vertical vorticity analysis. This circulation is not as intense as the mesovortex associated with the Omaha bow echo. The gradient of the single-Doppler velocity on the cold-air side of the outflow boundary (Fig. 11b) is weaker than the equivalent fields shown in Fig. 1. The highest wind speeds in Fig. 11b remain ~15 km to the west of the outflow boundary instead of wrapping around the mesovortex and producing an intense isotach gradient south of the circulation (see Figs. 1c and 5).

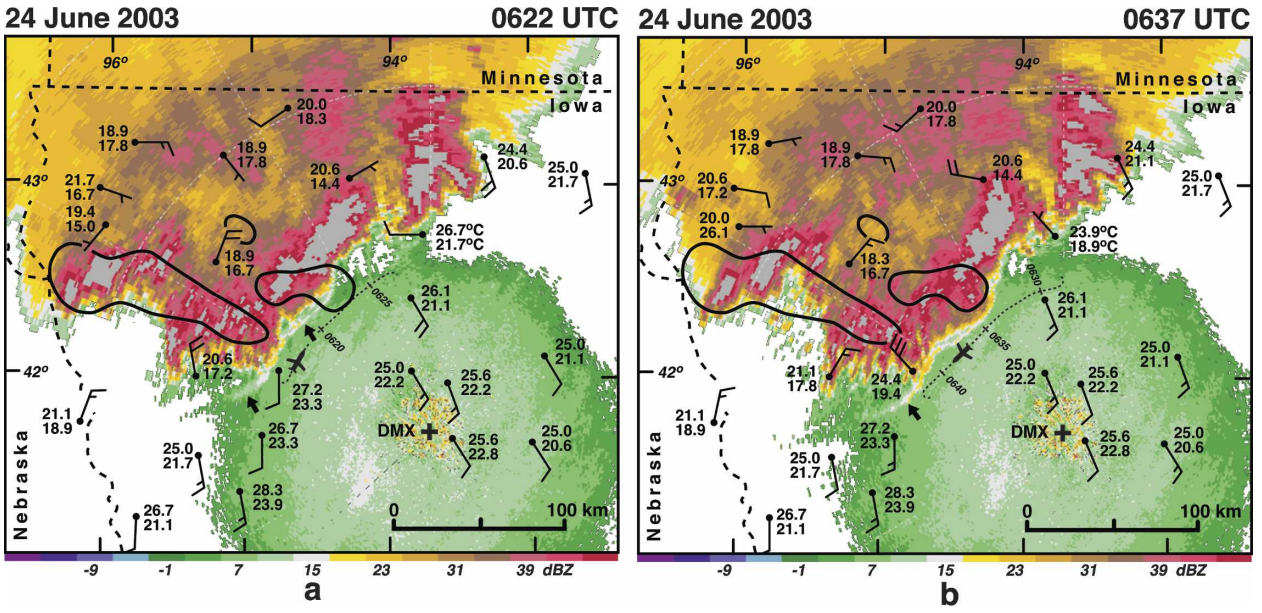

FIG. 9. Radar reflectivity from the DMX WSR-88D at (a) 0622 and (b) 0637 UTC. The black lines represent the extent of damage reported at the surface based on the analysis presented in Fig. 8. The dotted line represents the flight track of the NRL P-3. Surface reports of temperature, dewpoint temperature (°C), and wind speed and direction are plotted. The location of the radar is shown by the black cross. Wind vectors are plotted with the full barb and half-barb representing 5 and 2.5 m s^{-1}, respectively. The thick, dashed lines are the state borders. The black arrows denote the position of a thin line of radar reflectivity.

The surface damage created by the Storm Lake bow echo is different when compared with the Omaha bow echo. The latter was characterized by a narrow swath of high winds rated >F1 in damage intensity. This intense flow was embedded within a larger region of sporadic damage. The mesovortex was responsible for creating the damage swath while an intense, descending rear-inflow jet was responsible for the weaker damage spread over a larger region. In contrast, the damage associated with the Storm Lake bow echo appears to be primarily associated with a weaker rear-inflow jet. It is the combination of a weak rear inflow and mesovortex in this case that contributed to the absence of smaller-scale swaths of damaging winds.

7. Summary and discussion

A detailed analysis of the evolution of a mesovortex located near the apex of the Omaha bow echo was presented. The mesovortex originated as the cyclonic member of a vortex couplet that formed near the leading edge of an outflow boundary. The couplet was produced by tilting the horizontal baroclinic vorticity produced by the cold pool. The formation of vortex couplets rather than circulations of the same sign would appear to rule out horizontal shearing instability as the initiation mechanism. Downdrafts that were mechanically forced along the periphery of a developing cell provided the tilting mechanism as shown in Fig. 12. The origin of the downdraft is different than the one proposed by Trapp and Weisman (2003). They suggest that the downdrafts develop within precipitation from mature thunderstorms (see their Fig. 23). In the present case, storms initiated above the outflow boundary would not be able to produce a precipitation downdraft unless they were well to the rear of the gust front (Fig. 12).

The mesovortex intensified via vortex stretching and was located to the north of the region of damage rated >F1 in intensity. Trapp and Weisman (2003) hypothesize that intense mesovortices produce mesolows via the fluid shear terms in the diagnostic perturbation pressure equation. The horizontal pressure gradients that subsequently develop were proposed to be the primary forcing mechanism for the generation of strong surface winds. The current study suggests an alternative explanation.

The evidence presented in this paper supports the important role that mesovortices play in producing damaging straight-line winds. The pressure gradient forces accelerate the horizontal winds; however, intense mesovortices modify the low-level outflow and largely determine the locations where the strongest winds occur. The preferred regions can best be described as a

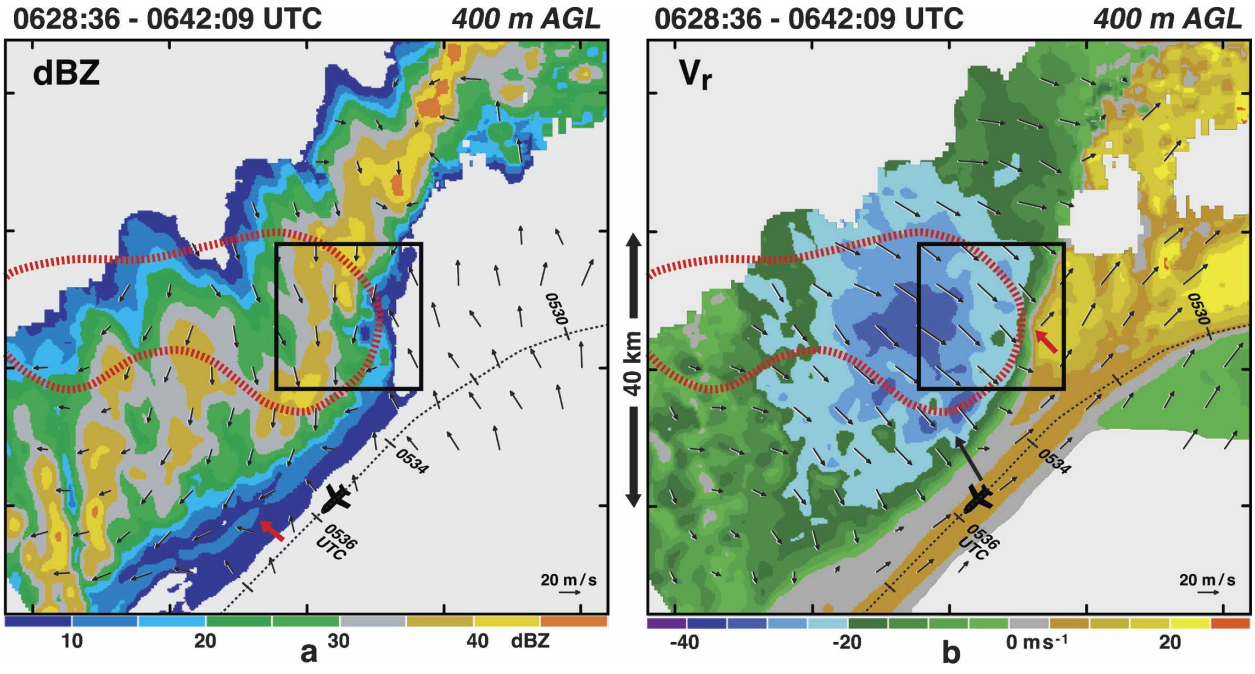

FIG. 10. Dual-Doppler wind synthesis at 0628:36–0642:09 UTC at 400 m AGL. (a) Storm-relative winds superimposed onto radar reflectivity and (b) ground-relative winds superimposed onto single-Doppler velocities. The dotted line represents the flight track of the NRL P-3. The damage at the surface is based on the results presented in Fig. 8 and is shown by the dashed red lines. The black box is enlarged in Fig. 11. The viewing angle of the radar is shown in (b). The red arrow in (a) indicates the position of a radar thin line. The red arrow in (b) indicates the position of a cusp-like feature in the single-Doppler velocity field.

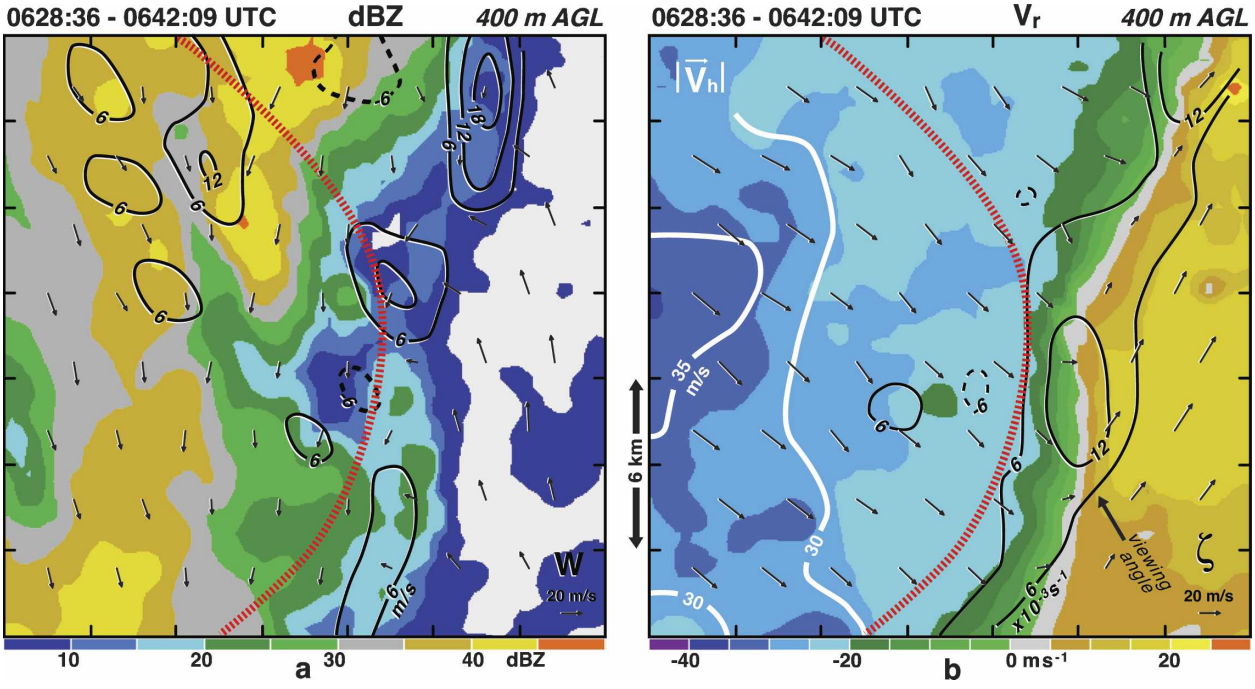

FIG. 11. Dual-Doppler wind synthesis at 0628:36–0642:09 UTC at 400 m AGL. (a) Storm-relative winds, and vertical velocities are superimposed onto radar reflectivity. (b) Ground-relative winds, vertical vorticity, and isotachs of horizontal velocity are superimposed onto single-Doppler velocities. The damage at the surface is based on the aerial and ground survey and is shown by the dashed red line. The location of the synthesis is shown in Fig. 10. The viewing angle of the Doppler radar is shown in (b).

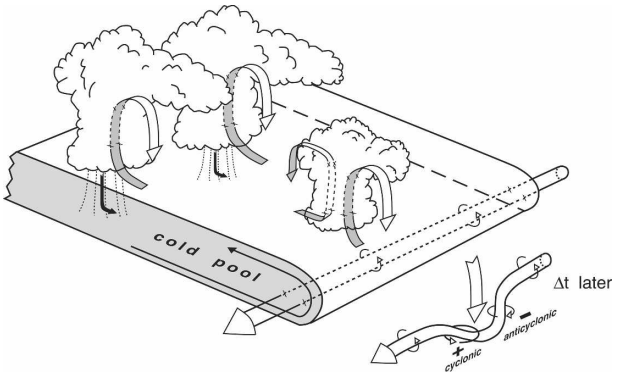

FIG. 12. Schematic model illustrating the origin of vortex couplets along the outflow boundary of the Omaha bow echo. The diagram at the bottom right represents the distortion of the vortex tube with increasing time.

superposition of the vortex and the flow in which it is embedded. This model explains the observed tongue of high wind speeds that were confined to the periphery of the mesovortex. It is also consistent with the air parcel trajectories, which do not follow a path along the maximum horizontal pressure gradient created by the mesolow. The strongest winds occur on the side of the vortex where translation and rotation effects are in the same direction. This finding supports the damage survey presented by Forbes and Wakimoto (1983). Several tornadoes documented in their study were accompanied by microburst damage located immediately to the south of the tracks (see Fig. 2 in Part I). It is also in agreement with the results from Atkins et al. (2005). Removal of the mesovortex circulation results in a displacement of the high winds to another location and over a greater area. The displaced isotachs of high wind speed appeared to be an extension of the descending rear-inflow jet.

Another bow echo event that occurred near Storm Lake, Iowa, was investigated in order to identify similarities and differences between the two cases. The Storm Lake bow echo produced damage over an extended region, but it was rated <F0 in intensity. Dual-Doppler wind syntheses suggest that the damage was largely associated with the descending rear-inflow jet. A mesovortex was resolved in the wind field but was too weak to have significantly impacted the outflow winds.

The results presented reveal the dominant effect that intense mesovortices have in producing jets of high wind speed. A key question that remains is the relationship between these intense mesovortices and bow echo tornadoes. Unfortunately, no multi-Doppler data were collected on a tornado spawned by a bow echo during BAMEX.

Acknowledgments. Dusty Wheatley and Jon Chamberlain participated in the ground survey of the damage produced by the 24 June bow echo. Research results presented in this paper were supported by the National Science Foundation under Grant ATM-021048 (through RMW) and ATM-0233178 (through NTA).

APPENDIX

Radar Methodology and Perturbation Pressure Retrieval

The ELDORA data were edited and the aircraft motion was removed from the velocity field using the Solo II software package (Oye et al. 1995). The data were then corrected for navigational errors using a technique developed by Testud et al. (1995). The along-track data spacing and sweep-angle beam spacing for ELDORA during BAMEX were ~300 m and 1.4°, respectively. The latter led to an effective sampling of ~400 m in the vertical within the smaller domain highlighted in this paper. Accordingly, the primary wind syntheses shown in this paper were interpolated onto a grid with a horizontal and vertical grid spacing of 300 and 400 m, respectively. A Cressman filter (Cressman 1959) was applied during the interpolation process with a radius of influence of 300 m in the horizontal and 400 m in the vertical. Sensitivity studies with larger radii of influence did not significantly alter the results. The lowest level was chosen to be at 300 m AGL.

The synthesis of the radar data was performed using the Custom Editing and Display of Reduced Information in Cartesian Space (CEDRIC; Mohr et al. 1986). A three-step Leise filter (Leise 1982) was applied to the Doppler wind field. This filter effectively removes wavelengths less than 2.4 and 3.2 km in the horizontal and vertical directions, respectively. In addition, horizontal and vertical wavelengths less than 4 and 5 km, respectively, are strongly damped. It is believed that the large time gap between synthesis times is partially mitigated by the larger resolvable scales. The hydrometeor fall speeds were estimated from the reflectivity–terminal fall speed relationship established by Joss and Waldvogel (1970), with a correction for the effects of air density (Foote and du Toit 1969). Vertical velocities were obtained from the horizontal convergence in a variational sense (O'Brien 1970) such that an integration of the anelastic continuity equation met both the upper and lower boundary conditions of $w = 0$ m s^{-1}.

Gal-Chen (1978) first proposed the use of three-dimensional winds synthesized from multi-Doppler radar analyses to retrieve the total perturbation pressure (p') and density patterns using a least squares method

in a horizontal plane. The retrieval treats the pressure and temperature as unknown variables and solves the Poisson equation derived from the anelastic momentum equation. While this method retrieves individual horizontal cross sections of perturbation pressure, it does not reveal its vertical structure.

Roux (1985, 1988), Roux and Sun (1990), and Roux et al. (1993) were able to modify Gal-Chen's method in order to retrieve the full three-dimensional perturbation pressure. This was accomplished by deriving a thermodynamic equation that relates the advection of temperature to the latent heat released through condensation or absorbed through melting and evaporation while neglecting other diabatic heat sources and sinks. It is assumed that saturated and unsaturated conditions occur during the production and removal of precipitation, respectively. The Roux technique, including the tendency term, is used in the present study.

A momentum check was performed to assess the quality of the retrievals. The values ranged from 0.18 to 0.24 for all of the analysis volumes shown in this paper, which is well within the acceptable range defined by Gal-Chen and Kropfli (1984). The momentum check is 0 when the wind field satisfies the anelastic vertical vorticity equation. Hence, the momentum check provides a dynamical constraint to the derived wind field that is more rigorous than the kinematic constraint (e.g., satisfying the mass continuity equation). The time gap between syntheses was 12–13 min. The retrievals presented in this paper were compared with the steady-state solutions (not shown) in order to assess whether these time gaps were too large to accurately estimate the tendency term. There were very small differences in the patterns and the individual values of the isopleths, suggesting that this effect was minimal although the values of the momentum check rose significantly. The latter is not surprising because the time evolution of the wind field needs to be included in order to produce the best retrievals.

REFERENCES

Atkins, N. T., J. M. Arnott, R. W. Przybylinski, R. A. Wolf, and B. D. Ketcham, 2004: Vortex structure and evolution within bow echoes. Part I: Single-Doppler and damage analysis of the 29 June 1998 derecho. *Mon. Wea. Rev.,* **132,** 2224–2242.

——, C. S. Bouchard, R. W. Przybylinski, R. J. Trapp, and G. Schmocker, 2005: Damaging surface wind mechanism within the 10 June 2003 Saint Louis bow echo during BAMEX. *Mon. Wea. Rev.,* **133,** 2275–2296.

Burgess, D. W., and B. F. Smull, 1990: Doppler radar observations of a bow echo associated with a long-track severe windstorm. Preprints, *16th Conf on Severe Local Storms,* Kananaskis Park, AB, Canada, Amer. Meteor. Soc., 203–208.

Carbone, R. E., 1982: A severe frontal rainband. Part I: Storm-wide hydrodynamic structure. *J. Atmos. Sci.,* **39,** 258–279.

Cressman, G. P., 1959: An operational objective analysis system. *Mon. Wea. Rev.,* **87,** 367–374.

Davis, C., and Coauthors, 2004: The Bow echo and MCV Experiment: Observations and opportunities. *Bull. Amer. Meteor. Soc.,* **85,** 1075–1093.

Foote, G. B., and P. S. du Toit, 1969: Terminal velocity of raindrops aloft. *J. Appl. Meteor.,* **8,** 249–253.

Forbes, G. S., and R. M. Wakimoto, 1983: A concentrated outbreak of tornadoes, downbursts, and microbursts, and implications regarding vortex classification. *Mon. Wea. Rev.,* **111,** 220–235.

Fujita, T. T., 1978: Manual of downburst identification for project NIMROD. University of Chicago SMRP Research Paper 156, 104 pp.

——, 1981: Tornadoes and downbursts in the context of generalized planetary scales. *J. Atmos. Sci.,* **38,** 1511–1534.

——, 1985: The downburst. University of Chicago SMRP Research Paper 210, 122 pp.

——, and H. R. Byers, 1977: Spearhead echo and downbursts in the crash of an airliner. *Mon. Wea. Rev.,* **105,** 129–146.

——, and R. M. Wakimoto, 1981: Five scales of airflow associated with a series of downbursts of 16 July 1980. *Mon. Wea. Rev.,* **109,** 1438–1456.

Funk, T. W., K. E. Darmofal, J. D. Kirkpatrick, V. L. DeWald, R. W. Przybylinski, G. K. Schmocker, and Y.-J. Lin, 1999: Storm reflectivity and mesocyclone evolution associated with the 15 April 1994 squall line over Kentucky and southern Indiana. *Wea. Forecasting,* **14,** 976–993.

Gal-Chen, T., 1978: A method for the initialization of the anelastic equations: Implications for matching models with observations. *Mon. Wea. Rev.,* **106,** 587–606.

——, and R. A. Kropfli, 1984: Buoyancy and pressure perturbations derived from dual-Doppler radar observations of the planetary boundary layer: Applications for matching models with observations. *J. Atmos. Sci.,* **41,** 3007–3020.

Heymsfield, G. M., and S. Schotz, 1985: Structure and evolution of a severe squall line over Oklahoma. *Mon. Wea. Rev.,* **113,** 1563–1589.

Holland, G. J., 1987: Mature structure and structure change. *A Global View of Tropical Cyclones,* R. L. Elsberry, Ed., Naval Postgraduate School, 13–52.

Houze, R. A., Jr., 1993: *Cloud Dynamics.* Academic Press, 570 pp.

Johns, R. H., and W. D. Hirt, 1987: Derechoes: Widespread convectively induced windstorms. *Wea. Forecasting,* **2,** 32–49.

Jorgensen, D. P., and B. F. Smull, 1993: Mesovortex circulations seen by airborne Doppler radar within a bow-echo mesoscale convective system. *Bull. Amer. Meteor. Soc.,* **74,** 2146–2157.

Joss, J., and D. Waldvogel, 1970: Raindrop size distribution and Doppler velocities. Preprints, *14th Conf. on Radar Meteorology,* Tucson, AZ, Amer. Meteor. Soc., 153–156.

Klemp, J. B., and R. Rotunno, 1983: A study of the tornadic region within a supercell thunderstorm. *J. Atmos. Sci.,* **40,** 359–377.

Knupp, K. R., and W. R. Cotton, 1985: Convective cloud downdraft structure: An interpretive survey. *Rev. Geophys.,* **23,** 183–215.

Lee, B. D., and R. B. Wilhelmson, 1997: The numerical simulation of non-supercell tornadogenesis. Part I: Initiation and evolution of pretornadic misocyclone circulations along a dry outflow boundary. *J. Atmos. Sci.,* **54,** 32–60.

Leise, J. A., 1982: A multidimensional scale-telescoped filter and data extension package. NOAA Tech. Memo. ERL WPL-82, 19 pp.

Miles, J. W., and L. N. Howard, 1964: Note on heterogeneous shear flow. *J. Fluid Mech.,* **20,** 331–336.

Mohr, C. G., L. J. Miller, R. L. Vaughn, and H. W. Frank, 1986: The merger of mesoscale datasets into a common Cartesian format for efficient and systematic analysis. *J. Atmos. Oceanic Technol.,* **3,** 143–161.

Mueller, C. K., and R. E. Carbone, 1987: Dynamics of a thunderstorm outflow. *J. Atmos. Sci.,* **44,** 1879–1898.

O'Brien, J. J., 1970: Alternative solutions to the classical vertical velocity problem. *J. Appl. Meteor.,* **9,** 197–203.

Oye, R., C. Mueller, and S. Smith, 1995: Software for radar translation, visualization, editing and interpolation. Preprints, *27th Conf. on Radar Meteorology,* Vail, CO, Amer. Meteor. Soc., 359–364.

Przybylinski, R. W., 1995: The bow echo: Observations, numerical simulations, and severe weather detection methods. *Wea. Forecasting,* **10,** 203–218.

Raymond, D. J., R. Soloman, and A. M. Blyth, 1991: Mass flux in New Mexico mountain thunderstorms from radar and aircraft measurements. *Quart. J. Roy. Meteor. Soc.,* **117,** 587–621.

Rotunno, R., J. B. Klemp, and M. L. Weisman, 1988: A theory for strong, long-lived squall lines. *J. Atmos. Sci.,* **45,** 463–485.

Roux, F., 1985: Retrieval of thermodynamic fields from multiple-Doppler radar data using the equations of motion and the thermodynamic equation. *Mon. Wea. Rev.,* **113,** 2142–2157.

——, 1988: The west African squall line observed on 23 June 1981 during COPT 81: Kinematics and thermodynamics of the convective region. *J. Atmos. Sci.,* **45,** 406–426.

——, and J. Sun, 1990: Single-Doppler observations of a west African squall line on 27–28 May 1981 during COPT 81: Kinematics, thermodynamics and water budget. *Mon. Wea. Rev.,* **118,** 1826–1854.

——, V. Marécal, and D. Hauser, 1993: The 12/13 January 1988 narrow cold-frontal rainband observed during MFDP/FRONTS 87. Part I: Kinematics and thermodynamics. *J. Atmos. Sci.,* **50,** 951–974.

Schmidt, J. M., and W. R. Cotton, 1989: A high plains squall line associated with severe surface winds. *J. Atmos. Sci.,* **46,** 281–302.

Shea, D. J., and W. M. Gray, 1973: The hurricane's inner core region. I. Symmetric and asymmetric structure. *J. Atmos. Sci.,* **30,** 1544–1564.

Smull, B. F., and R. A. Houze Jr., 1987: Rear inflow in squall lines with trailing stratiform precipitation. *Mon. Wea. Rev.,* **115,** 2869–2889.

Testud, J., P. H. Hildebrand, and W.-C. Lee, 1995: A procedure to correct airborne Doppler radar data for navigation errors using the echo returned from the earth's surface. *J. Atmos. Oceanic Technol.,* **12,** 800–820.

Trapp, R. J., and M. L. Weisman, 2003: Low-level mesovortices within squall lines and bow echoes. Part II: Their genesis and implications. *Mon. Wea. Rev.,* **131,** 2804–2823.

——, S. A. Tessendorf, E. S. Godfrey, and H. E. Brooks, 2005: Tornadoes from squall lines and bow echoes. Part I: Climatological distribution. *Wea. Forecasting,* **20,** 23–34.

Wakimoto, R. M., 1983: The West Bend, Wisconsin storm of 4 April 1981: A problem in operational meteorology. *J. Climate Appl. Meteor.,* **22,** 181–189.

——, 2001: Convectively driven high wind events. *Severe Convective Storms, Meteor. Monogr.,* No. 50, Amer. Meteor. Soc., 255–298.

——, and J. W. Wilson, 1989: Non-supercell tornadoes. *Mon. Wea. Rev.,* **117,** 1113–1140.

——, and P. G. Black, 1994: Damage survey of Hurricane Andrew and its relationship to the eyewall. *Bull. Amer. Meteor. Soc.,* **75,** 189–200.

——, H. V. Murphey, A. Nester, D. P. Jorgensen, and N. T. Atkins, 2006: High winds generated by bow echoes. Part I: Overview of the Omaha bow echo 5 July 2003 storm during BAMEX. *Mon. Wea. Rev.,* **134,** 2793–2812.

Weisman, M. L., 1992: The role of convectively generated rear-inflow jets in the evolution of long-lived mesoconvective systems. *J. Atmos. Sci.,* **49,** 1826–1847.

——, 1993: The genesis of severe, long-lived bow echoes. *J. Atmos. Sci.,* **50,** 645–670.

——, 2001: Bow echoes: A tribute to T. T. Fujita. *Bull. Amer. Meteor. Soc.,* **82,** 97–116.

——, and C. A. Davis, 1998: Mechanisms for the generation of mesoscale vortices within quasi-linear convective systems. *J. Atmos. Sci.,* **55,** 2603–2622.

——, and R. J. Trapp, 2003: Low-level mesovortices within squall lines and bow echoes. Part I: Overview and sensitivity to environmental vertical wind shear. *Mon. Wea. Rev.,* **131,** 2779–2803.

Wilson, J. W., and W. E. Schreiber, 1986: Initiation of convective storms at radar-observed boundary-layer convergence lines. *Mon. Wea. Rev.,* **114,** 2516–2536.

Yuter, S. E., and R. A. Houze Jr., 1995: Three-dimensional kinematic and microphysical evolution of Florida cumulonimbus. Part II: Frequency distributions of vertical velocity, reflectivity, and differential reflectivity. *Mon. Wea. Rev.,* **123,** 1941–1963.